
Article:
Aydin, A. orcid.org/0009-0007-3212-8040, Cetin, E., Erman, S.C. orcid.org/0000-0002-9615-5618 et al. (1 more author) (2025) Laser powder bed fusion of Ti6Al4V using low-cost high efficiency 450 nm diode point melting. Journal of Materials Research and Technology, 34. pp. 2814-2827. ISSN 2238-7854

https://doi.org/10.1016/j.jmrt.2024.12.252

Journal of Materials Research and Technology 34 (2025) 2814–2827

Contents lists available at ScienceDirect

Journal of Materials Research and Technology

journal homepage: www.elsevier.com/locate/jmrt

Laser powder bed fusion of Ti6Al4V using low-cost high efficiency 450 nm diode point melting

Alkim Aydin [a,b,*], Erhan Cetin [a,c], S. Can Erman [a], Kamran Mumtaz [a]

[a] School of Mechanical, Aerospace and Civil Engineering, The University of Sheffield, Sheffield, S1 3JD, United Kingdom
[b] Department of Automotive Engineering, Cukurova University, Adana, 01250, Turkiye
[c] Department of Mechanical Engineering, Hitit University, Çorum, 19030, Turkiye

ARTICLE INFO

Handling editor: L Murr

Keywords:
Additive manufacturing
Laser powder bed fusion
Ti6Al4V
Diode point melting (DPM)
Process optimization
Microstructure

ABSTRACT

Laser Powder Bed Fusion (LPBF) is a commonly used Additive Manufacturing (AM) method for the production of geometrically complex metal components that are used in high-value sectors. It uses high power fibre lasers directed by a galvanometric scanner to rapidly melt powdered feedstock. LPBF systems are expensive, making them inaccessible to many sectors and have challenges related to in-process thermal control, production of large components and scalability limitations. As an alternative to traditional LPBF, this study introduces Diode Point Melting (DPM), combining multiple low-power, energy efficient blue (450 nm) diode lasers into a single focal point. DPM's laser source is fixed to a scanning gantry axis that traverses across the powder bed, creating a low-cost alternative to traditional LPBF (~x10 lower laser hardware cost). DPM processes slower than LPBF, generating reduced thermal gradients with improved material laser energy absorption due to use of a shorter laser wavelength. DPM processing of Ti6Al4V was undertaken using 38W creating samples that were 99.41% dense. DPM's slower melt pool solidification rate enabled the formation of a stable $\alpha + \beta$ phase creating harder samples. The grain size of Ti6Al4V samples fabricated using DPM were significantly larger compared to those produced by LPBF (grain size area ~ x30 larger). Young's modulus of the samples produced via DPM was found to be higher than LPBF manufactured Ti6Al4V, indicating increased stiffness. DPM is a promising low-cost alternative to LPBF, offering the opportunity to make net-shape metal AM more widely accessible in both academic and industrial sectors.

1. Introduction

Additive manufacturing (AM) offers numerous advantages over conventional manufacturing techniques, including greater geometric flexibility, reduced material waste, the ability to consolidate multiple components into a single structure, and the capacity for customisation without incurring additional costs [1–3]. The most widely used AM method in the industry is the Laser Powder Bed Fusion (LPBF) technique. LPBF is a metal AM technique that builds high-density components with fine microstructures by selectively melting layers from different engineering alloys (e.g., Ti6Al4V [4], Inconel [5], AlSi10Mg [6], 316L stainless steel [7], CoCr [8]). This layer-by-layer process allows for the creation of fully dense, complex parts while minimising material waste. Ti6Al4V components made through LPBF are highly valued in used in high value sectors in aerospace, energy, and medical due to their lightweight, durable properties, and ability to meet complex design requirements [4,9,10]. However, LPBF systems have notable drawbacks, including the high investment and operating costs, scalability and components size limitation, post-processing requirements for finished parts, and limited laser absorptivity for most metals (for example, aluminium alloys absorb less than 10%, whereas titanium absorbs 50–60%, for the wavelength of 1064 nm typically used in LPBF) and need for high laser power. Moreover, high-intensity lasers moving at high speeds can generate substantial thermal gradients, which can lead to defects in parts should as cracks and warpage [11,12]. An alternative to LPBF galvo-scanning approach has been investigated, a gantry system (a Cartesian motion system) where multiple 976 nm fibre coupled lasers are mounted and traverse a powder bed was investigated by Karp et al. [13] The system also includes extra motion axes, such as a vertical stage to fine-tune the focus position at the working plane and a rotation stage at the v-groove to adjust the orientation of the fibre array. The gantry system enables synchronised motion across the laser channels, which

* Corresponding author. School of Mechanical, Aerospace and Civil Engineering, The University of Sheffield, Sheffield, S1 3JD, United Kingdom.
E-mail addresses: alkaydin@gmail.com, a.aydin@sheffield.ac.uk (A. Aydin).

https://doi.org/10.1016/j.jmrt.2024.12.252
Received 12 November 2024; Received in revised form 28 December 2024; Accepted 29 December 2024
Available online 30 December 2024

Table 1
Composition of elements in the Ti6Al4V powder material supplied by Carpenter Additive.

Ti	Al	V	O	N	H	Fe	C	Others
Balance (wt. %)	5.91	3.88	0.07	0.01	0.002	0.19	<0.01	0.40

compensates for the slower scanning speeds (i.e., 300 mm/s) by covering a wider area. A 16-channel laser array, with a combined output of up to 960W (sixteen 60 W, 976 nm diode modules), was demonstrated to achieve part densities greater than 99% at 2x the build rate of conventional single-laser systems using CoCr powder. Additionally, Bernsmann et al. [14] explored the use of a gantry system in LPBF as a cost-effective alternative to conventional methods. The gantry system, although slower than conventional galvo-scanners, proved capable of guiding the laser effectively, enabling the production of stable builds even at reduced speeds. In their system, a gantry setup incorporating a 200 W multi-mode fibre laser with a wavelength of 1070 nm and allowing scanning speeds of up to 150 mm/s was utilised. Although the scanning speed was relatively low, samples achieving up to 99.84% relative density were still produced. Furthermore, Zavala-Arredondo et al. [15] introduced an alternative innovative technology, known as Diode Area Melting (DAM), that involves employing individually addressable diode lasers with a shorter wavelength of 808 nm and lower optical outputs, specifically between 3 and 5 W, mounted within a gantry system, as opposed to the high-power fibre lasers and galvanometer scanners commonly used in conventional LPBF systems. Using the DAM approach, Alsaddah et al. [16] also successfully produced Ti6Al4V samples with over 90% relative density by employing two different wavelength lasers, 450 nm, and 808 nm, with a laser power of only 3.5 W. The study revealed that the absorption when processing Ti6Al4V was 11% greater with 450-nm lasers compared to 808-nm lasers and 14% higher than with 1064-nm lasers. Similarly, Caglar et al. [17] used multiple low-power (4 W) 450 nm diode lasers to produce high-dense Ti6Al4V samples. They achieved 99.3% relative density in their samples and reduced hardness by around 40% through the application of a rescanning strategy. When comparing the relatively new DAM process with conventional LPBF systems in terms of build rate, although DAM, with a rate of 0.104 cm^3/hr [17], is currently much slower than LPBF, which has a rate of 1–100 cm^3/hr [18], this scanning speed leads to a lower solidification rate of 750–1400 °C/s [16], compared to the LPBF cooling rates of 10^5–10^7 °C/s. In studies by Hooper et al. [19], Yang et al. [20], and Gong et al. [21], the cooling rates were measured as 1-40x10^6 K/s, 10^{5-6} K/s, and 10^{4-6} K/s respectively. During the rapid solidification and cooling processes characteristic of LPBF, the body-centered cubic (bcc) β phase in the Ti6Al4V alloy fully transforms into a metastable hexagonal close-packed (hcp) α′ martensite phase through a diffusionless shear transformation mechanism. As a result, the microstructure comprises very fine α′ martensite within columnar prior β grains [22]. These columnar β grain boundaries, while certainly enhancing the material's strength and hardness [9], also promote intergranular failure, which orchestrates a reduction in ductility [23].

LPBF machines are predominantly equipped with fibre lasers (with a wavelength of 1064 nm), along with galvanometric scanners to direct the beam to the desired area, both of which are expensive components ($15–50K) [14]. In addition, due to the movement limitations of optical mirrors and beam quality, the processing size over a powder bed is restricted. Moreover, the 1064 nm wavelength that fibre lasers operate at cause much of the laser's energy to be reflected rather than absorbed, particularly with copper [24] and gold [25]. Furthermore, the rapid laser movement results in high cooling rates, which reduces the ductility of materials and leads to increased brittleness. Motivated by these issues, an alternative manufacturing approach referred to as Diode Point Melting (DPM), is proposed in this work. This study employs a short-wavelength (i.e., 450 nm), low-power (i.e., 43.5 W) diode laser, along with a gantry system for its movement. This method integrates several low-power diode lasers (each of 5.5 W) at a single focal point, offering a more affordable and accessible alternative to conventional LPBF. The laser source, power control, and cooling costs less than $1500. DPM's total cost could be much less than commercially available LPBF systems, primarily due to the use of a low-cost 450 nm diode laser on traversing axis. Additionally, DPM's scalability allows for the production of larger components, such as bicycle frames, which are challenging to create with LPBF due to the limited distance the laser is allowed to travel from galvo-mirror/f-theta lens center before beam degradation takes place. This study investigates part properties and optimal process parameters for processing of Ti6Al4V using DPM, exploring influence of laser processing hatch distance, layer thickness, laser power, and production with/without supports.

Table 2
Physical properties of the Ti6Al4V powder material [26].

Material	Ti6Al4V Powder
Absorptivity (A)	0.72 (450 nm wavelength)
Thermal conductivity (λ)	7.2 W/m.K (at 298 K)
Material density (p)	4420 kg/m^3
Specific heat (C_P)	560 J/kg.K in (283–923 K)

2. Materials and methods

All the experiments are conducted on Ti6Al4V Grade 5 ELI23 powder, supplied by Carpenter Additive. The powder is produced by the gas atomisation method with the batch number PR100548. Tables 1 and 2 show the composition of elements calculated by the ASTM F3001 method in the Ti6Al4V powder material.

The particles are produced in spherical morphology and size range specified as 15–45 μm. The size distribution determined by the manufacturer with ASTMB822 standard and given by size quantiles Dv (10) = 17.4 μm, Dv (50) = 30.8 μm, Dv (90) = 51.6 μm. The hall flowability with ASTM B213 standard is represented to be 37.00 s/50g and apparent density 2.21 g/cm^3 according to the manufacturer test report. Fig. 1a represents the particle size distribution according to the Malvern Mastersizer 3000 result. Fig. 1b shows an SEM (Scanning Electron Microscopy) image of virgin Ti6Al4V powder. It can be clearly seen that particles match the spherical morphology with a small amount of irregular near-spherical particles.

The experiments are conducted on The University of Sheffield's developed Diode Area/Point Melting machine, named DAMX (developed under the EPSRC's Novel Manufacturing Instrumentation call). This machine has an integrated gantry system in the build chamber that gives an allowance to attach the DPM laser. The platform has an argon gas recirculation system which continuously feeds argon gas into the build area. Oxygen level is continuously monitored with an Atlas Scientific EZO-O2™ embedded oxygen sensor. During the experiments O_2 level are maintained below 1000 ppm. Fig. 2 represents the general view of the in-house developed DAMX machine and its inner printing platform. Laser power, layer thickness, hatch distance, additional support structures, and laser speed are considered process parameters. In this context, the Ti6Al4V samples are produced using two different laser power (19 W and 38 W), four different layer thicknesses (30, 60, 90, and 120 μm), four different hatch distances (50, 75, 100, and 125 μm) and two different support conditions (with/without support) under various laser scanning speeds.

The laser system used in the experiments has a total power output of

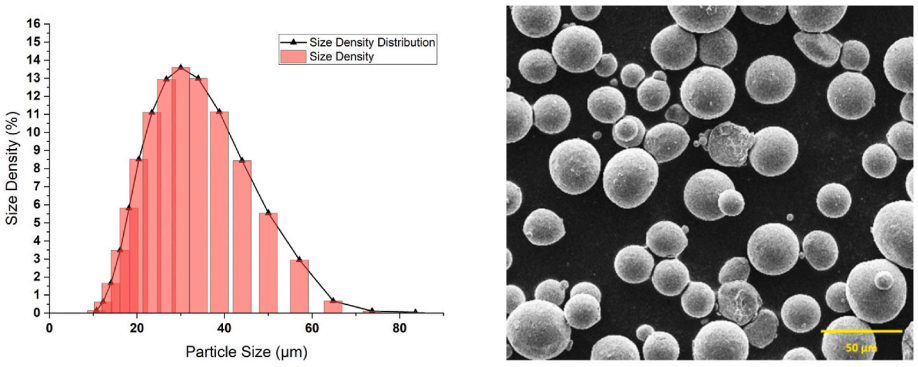

Fig. 1. a) Powder size distribution graph and b) SEM image of Ti6Al4V.

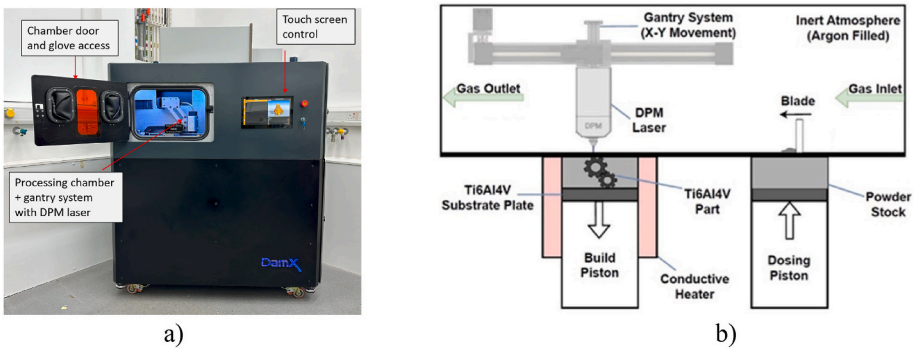

Fig. 2. a) The University of Sheffield DAMX machine and b) schematic of inner chamber.

43.5 W. During testing, the laser is operated at 85% of its maximum power (38 W) giving a constant laser power output during power delivery. The laser spot size is measured to be 100 × 150 μm. This is achieved by combining the output of eight individuals 5.5 W, 450 nm diode lasers, which are focused into a single spot. Cube specimens are produced with dimensions of 8 × 8 × 5 mm^3. For each case, at least three samples are produced for repeatability. After manufacturing each specimen, the specimens are cleaned by using an ultrasonic cleaner and isopropanol. The top surface roughness (Ra) of the produced samples is examined optically using Alicona Infinite Focus SL using the following formula.

$$Ra = \frac{1}{L}\int_0^L |Z(x)|dx \quad (1)$$

where L denotes the sampling length, and Z(x) represents the profile height at position x. For the microhardness testing Zwick Roell Durascan machine is used to measure the Vickers hardness values. Throughout all the tests, a load of 1.0 kgf is applied, and five different measurements are taken for each sample in every test. For the microscopic examination, the specimens are externally mounted with bakelite by using Buehler Simplimet Mounting Press. After the mounting, grinding, and polishing operation is used via the Buehler Automet machine. 320/600/1200/2400 and 4000 grit paper is used accordingly to complete the grinding. For polishing 90% of 0.06 μm colloidal suspension with combination of 10% hydrogen peroxide (H_2O_2) solution is used for polishing. In the final step before optical microscopy, all the samples are rinsed with water in Automet machine and cleaned with isopropanol. Nikon LV150NL optical microscope is used for capturing the density maps. Also with polarised filters, some microstructures are observed successfully. ImageJ software [27] is used to determine the density and porosity size measurements. It is a widely utilised software for determining the density and porosity sizes of LPBF samples using analysing optical images. High-resolution images of sample cross-sections, obtained via Nikon LV150NL microscopy, are post-processed in ImageJ through grayscale conversion and noise reduction. Thresholding techniques are then used to segment pores from the solid material, resulting in binary images in which porosity is quantified as the percentage of black pixels relative to the total image area. It should be noted that the same threshold values are used to get more accurate results for all samples. The relative density is calculated as 100% minus the porosity percentage, with results averaged from all cross-section regions to ensure accuracy. Also, for the porosity sizes measurements, 10 randomly pores are selected and measured to achieve more accurate results. Porosity sizes greater than 10 μm are typically classified as lack-of-fusion porosities, characterized by irregular shapes, with measurements taken along the major axis. Conversely, porosities smaller than 10 μm are classified as gas pores, which generally exhibit circular shapes, with measurements based on their diameters [28–32]. The measurement approach was determined by the shape of the pores, using either the major axis or the diameter as appropriate.

A JEOL-7900F Schottky Field Emission Scanning Electron Microscope is employed to perform Electron Backscatter Diffraction (EBSD) analysis for the purpose of examining the crystallography and mechanical properties of the Ti6Al4V samples. Before the EBSD analysis, PECS argon ion beam system is used to fully remove any unwanted colloidal silica or any unwanted particles. With JEOL-7900F, an area of 0.30 x 0.40 mm^2 on the YZ plane has scanned with a step size of 250 nm. To reconstruct the parent β grains, the Burgers orientation relationship is applied, specifically $\{0111\}\alpha//\{110\}\beta$ and $\langle 11\bar{2}0\rangle\alpha//\langle 111\rangle\beta$. The software Aztec Crystal is utilized to generate pole figures (PFs) using equal-area projection, marked by a half-width of 10 degrees and scaled in multiples of random density. Additionally, the software facilitated inverse pole figure (IPF) mapping, parent β grain reconstruction, and grain size analysis. A misorientation threshold of 10° is established to

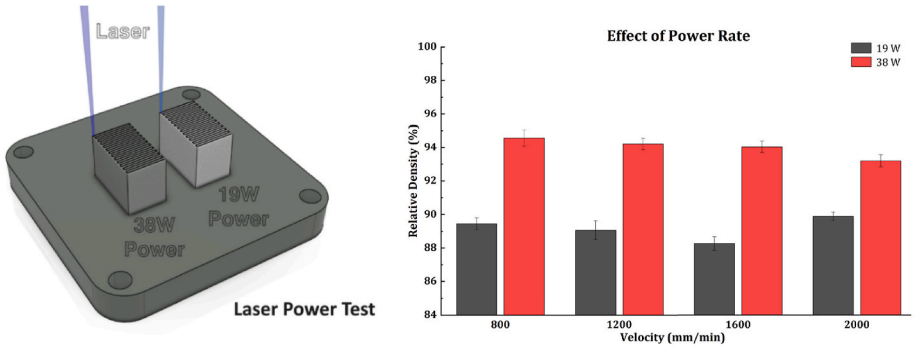

Fig. 3. a) Laser power test illustration and b) effect of power rate comparison chart.

differentiate between sub-grains.

Normalised energy density (NED) calculations are employed for all multilayer experiments in this study. To examine only the top surface roughness and single surface conditions, surface energy density (SED) is also utilised to create an ideal comparison chart. The formulas represent the definition and explanation of SED, VED (volumetric energy density) and NED calculations.

$$SED = E_s = \frac{P}{v \times h} \tag{2}$$

where *P, v* and *h* stand for output laser power (W), scan speed (mm/min), and hatch distance (mm), respectively.

$$VED = E_v = \frac{P}{v \times h \times l} \tag{3}$$

where *l* stands for the layer height of the powder (mm).

$$NED = E_n = \frac{P^*}{v^* \times l^* \times h^*}\ [33] \tag{4}$$

$$P^* = \frac{A \times q}{r_B \times \lambda \times (T_M - T_0)} \quad v^* = \frac{v \times r_B}{\alpha} \quad l^* = \frac{2 \times l}{r_B} \quad h^* = \frac{h}{r_B} \tag{5}$$

$$NED = E_n = \frac{P^*}{v^* \times l^* \times h^*} = \left[\frac{\frac{A \times P}{r_B \times \lambda \times (T_M - T_0)}}{\frac{v \times r_B}{\alpha} \times \frac{2 \times l}{r_B} \times \frac{h}{r_B}}\right] = \left[\frac{A \times P \times \alpha}{2 \times \lambda \times v \times l \times h \times (T_M - T_0)}\right] \tag{6}$$

$$\alpha = \frac{\lambda}{p \times C_P} \tag{7}$$

$$NED = E_n = \frac{P^*}{v^* \times l^* \times h^*} = \left[\frac{A \times P}{2 \times v \times l \times p \times h \times C_P \times (T_M - T_0)}\right] \tag{8}$$

Where *A* is absorptivity, α is thermal diffusivity (m^2/s), *v* scanning speed (m/s), *l* is layer height (m), *p* is material density (kg/m^3), *h* is hatch distance (m), C_P is the specific heat capacity of the powder (J/kg.K), T_M is the melting temperature of powder (K), T_0 is the powder bed temperature (K), r_B is the laser beam spot radius (m), λ is thermal conductivity (W/m.K). NED graph for ideal material melting regions can be found in the literature works [33].

SED and NED quantify energy densities in two and three dimensions, respectively. In LPBF, various process parameters significantly influence the characteristics of the final product [34]. Despite this complexity, it is commonly recommended to focus on one or two key parameters. The primary parameters in LPBF laser power, scan speed, hatch distance, and layer height collectively determine the VED utilised in the process. VED is frequently employed as a benchmark for optimising these parameters due to its comprehensive integration of these four critical factors.

Guo et al. [35] argued that variations in laser absorption, particularly at a constant input energy density, substantially affect melt pool dynamics. This absorption variability stems from the differing impacts of laser power and scan speed on the formation of the deepening zone during melt pool solidification. It was demonstrated that changes in energy absorption rates, even with constant VED levels, result in variations in the melt pool. Specifically, at a constant VED, an increase in energy absorption occurs when both laser power and scan speed are simultaneously elevated. When high energy density is applied, particularly to alloys with low melting point elements, several detrimental effects can occur. Excessive energy input may cause overheating and evaporation of these low-melting-point elements, thereby altering the alloy's chemical composition. This can lead to issues such as increased porosity, the formation of undesirable phases, and a reduction in mechanical properties. Additionally, high energy density can enlarge the heat-affected zone, exacerbating residual stresses and distortion in the final component [36–38].

Although VED is explanatory in many aspects, it was found that VED does not sufficiently explain melt pool physics or predict laser-powder interactions [38,39]. Thomas et al. [33] conducted a comprehensive analysis of the factors influencing the microstructure of LPBF-produced parts and introduced the concept of NED. This analysis considered factors such as beam quality, focusing, wavelength, scanning strategy, oxygen levels in the chamber, powder-specific heat capacity (C_P), single laser beam radius (r_B), thermal conductivity (λ), diffusivity (α), material density (*p*), and other relevant parameters. Specific parameters included melting temperature (T_M), powder-bed temperature (T_0), layer height (l) and its normalised version (l*), hatch distance (h) and its normalised version (h*), laser power (q) and its normalised version (q*) and scanning speed (ν) and its normalised version (v*). This research demonstrated that dimensionless parameter groups offer a more comprehensive explanation than VED.

3. Results

All the process optimisations start with the investigation of laser power effect on relative density results. The main objective of the optimization of process parameters is to obtain the best parameters that could reduce the overall printing time without losing the densification, achieving high surface accuracy parts, and to keep microhardness values above a certain level. After the power level investigation, the research moved on to an effect on layer thickness and followed up with hatch distancing and support structure accordingly. In this work, LH represents layer height (unit: μm), HD represents hatch distance (unit: μm), P represents laser power (unit: W) and V represents scanning velocity (unit: mm/min) in the following results section.

Table 3
Effect of power rate overall comparison result table.

Specimen name	NED	Relative density (%)	Porosity Sizes (μm)
60LH, 100HD, 19P, 800V	42.64	89.44	56.50 (±19.74)
60LH, 100HD, 19P, 1200V	28.43	89.06	55.10 (±11.76)
60LH, 100HD, 19P, 1600V	21.32	88.26	51.50 (±16.53)
60LH, 100HD, 19P, 2000V	17.06	89.89	50.60 (±12.89)
60LH, 100HD, 38P, 800V	85.29	**94.56**	46.60 (±20.04)
60LH, 100HD, 38P, 1200V	56.86	**94.20**	44.00 (±14.72)
60LH, 100HD, 38P, 1600V	42.64	**94.04**	40.10 (±10.80)
60LH, 100HD, 38P, 2000V	34.12	**93.20**	38.40 (±11.36)

3.1. Effect of laser power

In this section, the effects of Ti6Al4V samples produced with two different laser powers on relative density are examined. The laser used in this study has a maximum power output of 43.5 W. To assess the effect of laser power on the relative density of the samples, two power levels, 38 W and 19 W, are selected. Operating at the maximum power output of 43.5 W could potentially damage the laser over extended use; therefore, 38 W (85% of overall power) is chosen as a near-maximum level. Additionally, 19 W is selected as half of this power setting to enable a comparative analysis at reduced power. Laser power test illustration and power rate – relative density comparison chart of samples produced is presented in Fig. 3a and b, respectively.

It should be also noted that in order to better understand the effect of laser power, constant hatch distance and layer height values are taken into account. The layer thickness and hatch distance values are selected based on a review of the existing literature on the processing of Ti6Al4V using traditional LPBF techniques. The values in the literature demonstrate fluctuations for Ti6Al4V, with a range of 30–60 μm [40–43] and 50–160 μm [41,42,44,45], respectively for layer thickness and hatch distance. Therefore, the layer thickness of 60 μm and hatch distance of 100 μm are selected. For all samples in Fig. 3b, it is observed that the samples produced with 38 W laser power have better relative density values than the samples produced with 19 W. According to the figure, all the samples with a relative density of 90% and above are obtained with 38 W. The porosity analysis reveals a notable influence of laser power and scanning speed on pore size. At 19 W laser power, pore sizes demonstrate a slight reduction with increasing scanning speed, while at 38 W laser power, a significant decrease in pore size is observed across all speeds. This indicates that higher laser power effectively minimizes porosity, aligning with the overall trend of reduced porosity rates correlating to smaller pore sizes. For both laser power settings, the observed pores exhibit irregular shapes, which are characteristic of porosity caused by a lack of fusion [28–32]. As expected, this revealed that high laser power has a significant effect on the relative densities of the samples compared to low laser power. Furthermore, the LPBF study revealed that an increase in laser power from 100W to 200W result in a notable reduction in pore size, from 390 to 360 μm, and a considerable decrease in the volumetric ratio of porosity, from 0.27 to 0.02% [46]. In addition, Khorasani et al. [47] linked a reduction in laser power with a lack-of-fusion error resulting from a decline in temperature within the melt pool. Additionally, no significant correlation was observed between the laser power and scanning speed difference. NED values of the samples in also presented in Table 3. According to the table, it was observed that the samples with the highest relative density values (above 90%) are obtained in the samples with NED values between 34 and 86.

3.2. Effect of layer thickness

In this section, the effects of different layer thicknesses on the relative density and NED values of the samples are examined. In this context, four different layer thickness values were considered: 30, 60, 90 and 120 μm. Layer thickness test illustration and layer height - relative density comparison chart is presented in Fig. 4a and b, respectively. It should also be noted that constant hatch distance and laser power values are taken into account in order to better understand the effect of layer height and thickness. Since it is seen in the previous section that the cases with the highest relative density are in the samples with a laser power of 38W, the laser power is selected as a constant 38 W in this section. It is also clearly seen from Fig. 4b that the samples with the highest relative density value are the samples with a layer thickness of 30 μm. The layer height from 30 μm to 120 μm generally leads to a decrease in relative density from 98.79% to 89.30% and an increase in porosity size from about 19.20 μm (±8.70) to 73.00 μm (±19.24) (see Table 4). This trend suggests that thicker layers may result in incomplete melting and bonding, thereby reducing density and enlarging porosity. At higher relative densities, porosity typically comprises a mix of gas-induced pores and lack-of-fusion defects. Gas porosities are generally spherical and result from entrapped gases during rapid solidification.

Table 4
Effect of layer height overall comparison result table.

Specimen name	NED	Relative density (%)	Porosity Sizes (μm)
30LH, 100HD, 38P, 800V	85.29	**97.81**	28.40 (±13.39)
30LH, 100HD, 38P, 1200V	56.86	**98.38**	19.80 (±6.76)
30LH, 100HD, 38P, 1600V	42.64	**98.79**	19.20 (±8.70)
30LH, 100HD, 38P, 2000V	34.12	**97.66**	32.40 (±13.85)
60LH, 100HD, 38P, 800V	42.64	94.56	46.60 (±20.04)
60LH, 100HD, 38P, 1200V	28.43	94.20	44.00 (±14.72)
60LH, 100HD, 38P, 1600V	21.32	94.04	40.10 (±10.80)
60LH, 100HD, 38P, 2000V	17.06	93.20	38.40 (±11.36)
90LH, 100HD, 38P, 800V	28.43	90.32	54.30 (±7.09)
90LH, 100HD, 38P, 1200V	18.95	90.91	58.50 (±15.20)
90LH, 100HD, 38P, 1600V	14.21	92.02	51.50 (±12.62)
90LH, 100HD, 38P, 2000V	11.37	93.32	47.20 (±19.61)
120LH, 100HD, 38P, 800V	21.32	92.35	71.20 (±22.93)
120LH, 100HD, 38P, 1200V	14.21	90.62	73.00 (±19.24)
120LH, 100HD, 38P, 1600V	10.66	89.30	67.20 (±23.04)
120LH, 100HD, 38P, 2000V	8.53	90.66	67.30 (±22.77)

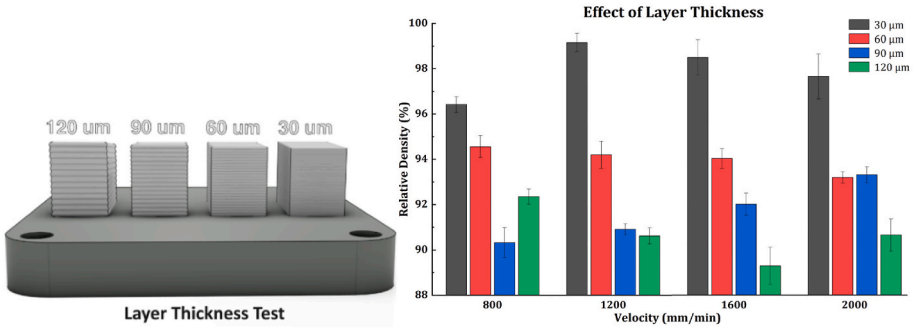

a) b)

Fig. 4. a) Layer thickness test illustration and b) effect of layer height comparison chart.

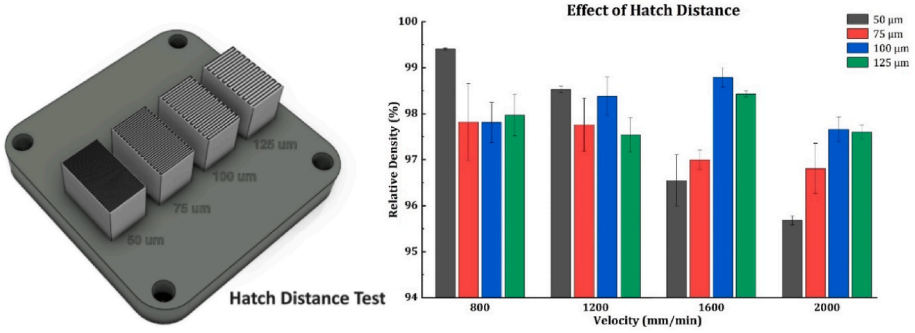

Fig. 5. a) Hatch distance test illustration and b) Effect of hatch distance comparison chart.

Table 5
Effect of hatch distance overall comparison result table.

Specimen name	NED	Hardness (HV)	Relative density (%)	Porosity Sizes (µm)
50HD, 30LH, 38P, 800V	170.58	**392.8**	**99.41**	14.10 (±4.98)
50HD, 30LH, 38P, 1200V	113.72	388.1	**98.53**	25.40 (±10.45)
50HD, 30LH, 38P, 1600V	85.29	386.9	96.55	32.00 (±12.14)
50HD, 30LH, 38P, 2000V	68.23	383.9	95.68	45.70 (±19.17)
75HD, 30LH, 38P, 800V	113.72	**392.6**	97.82	31.90 (±14.26)
75HD, 30LH, 38P, 1200V	75.81	381.8	97.76	30.40 (±14.66)
75HD, 30LH, 38P, 1600V	56.86	383.6	97.00	38.10 (±15.62)
75HD, 30LH, 38P, 2000V	45.49	**405.8**	96.81	40.60 (±15.11)
100HD, 30LH, 38P, 800V	85.29	377.9	97.81	28.40 (±13.39)
100HD, 30LH, 38P, 1200V	56.86	378.8	**98.38**	19.80 (±6.76)
100HD, 30LH, 38P, 1600V	42.64	367.4	**98.79**	19.20 (±8.70)
100HD, 30LH, 38P, 2000V	34.12	383.7	97.66	32.40 (±13.85)
125HD, 30LH, 38P, 800V	68.23	373.0	97.97	27.90 (±13.68)
125HD, 30LH, 38P, 1200V	45.49	360.8	97.54	25.50 (±8.73)
125HD, 30LH, 38P, 1600V	34.12	378.4	**98.43**	26.70 (±12.37)
125HD, 30LH, 38P, 2000V	27.29	**394.8**	97.60	34.40 (±9.49)

Lack-of-fusion porosities, often irregular in shape, occur due to insufficient melting between layers or scan tracks. As relative density decreases, the overall porosity size tends to increase, with a notable reduction in gas porosities. This shift suggests that, at lower densities, the predominant porosity type is lack-of-fusion defects, which are larger, and more irregular compared to gas pores [28–32]. With this approach, the porosity analysis reveals that at a layer height of 30 µm, both gas porosity and lack of fusion porosity are observed. However, as the layer height increases from 60 µm to 120 µm, all identified porosity features are predominantly categorized as lack of fusion porosity [28–32]. It is demonstrated that a significant number of studies yielding relative densities above 99.5% are conducted with a layer height of 30 µm in the literature [42,48,49]. In particular, it is found that the sample with the highest relative density value among all samples is the sample with 98.79%, 30 µm layer height, and 1600 mm/min scanning speed.

In Table 4, NED values are given according to different scanning speed for different layer thickness values. It is observed that the NED values of the samples with the highest relative density values are found to be between 34 and 86, which is consistent with previous observations (see Table 3). Furthermore, the relative density results of two samples in the same energy states (42.64, Table 4) demonstrate discrepancies, with values of 98.79% and 94.56%, respectively, for 30LH and 60LH. A reduction in layer thickness results in an increase in relative density, a finding that is corroborated by a review of the literature on LPBF. Greco et al. [50] posited that selecting a layer thickness of 25 µm instead of 35 or 45 µm at an equivalent energy state results in an enhanced density of the samples.

3.3. Effect of hatch distance

3.3.1. Relative density

In this section, the effects of different hatch distances on the relative densities of the samples are examined. In this context, four different hatch values are considered: 50, 75, 100, and 125 µm. Since it is seen in the previous section that the cases with the highest relative density were in the samples with a layer thickness of 30 µm, the layer thickness is chosen as constant and 30 µm in this section. In Fig. 5a, the hatch distance test illustration, and in Fig. 5b, relative density values of samples with different hatch values are presented according to various speed values.

As can be clearly seen from Fig. 5b and Table 5, the sample with the highest relative density is the structure with a hatch distance of 50 µm, layer thickness of 30 µm, laser power of 38 W, and scanning speed of 800 mm/min. It can be hypothesised that a reduction in hatch distance should result in an increase in relative density and reducing porosity sizes due to enhanced melt pool overlap [51]. It was observed that there is no significant correlation between hatch distance values and relative density. As the hatch distance is increased from 50 µm to 75 µm, a corresponding decrease in relative density is observed, by the findings of previous literature. However, an additional increase in hatch distance to 100 µm from 75 µm yields a denser result. This behavior has also been documented in one of the literature LPBF works concerning the processing of Inconel 718 [52]. Besides, a low hatch distance value significantly decreases production speed, adversely affecting both time and cost efficiency. To illustrate, a sample with a 50 µm hatch distance and a scanning speed of 800 mm/min exhibits a relative density that is 0.62% higher than that of a sample with a 100 µm hatch distance and a scanning speed of 1600 mm/min. The printing time for a single layer is increased threefold. In addition, the sample exhibited a relative density exceeding 99% with a 100 µm hatch distance and a scanning speed of 1600 mm/min. These parameters are achieved through the utilisation of a support structure, the specifics of which will be discussed later in this paper. In addition to the relative density calculations, this study examines hardness values and top surface roughness respectively. Subsequently, the discussion concentrates on the hardness and surface

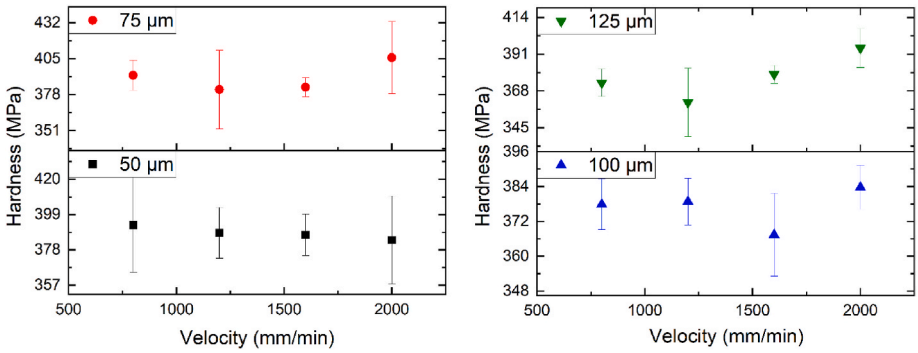

Fig. 6. Hardness values of the Ti6Al4V samples for different hatch distances.

roughness measurements of samples with varying energy density values. It is found from Table 5 that the sample with the highest hardness value is the sample with a hatch distance of 75 µm, layer thickness of 30 µm, laser power of 38 W, and scanning speed of 2000 mm/min.

3.3.2. *Microhardness measurements*

In assessing the microstructure of materials produced through LPBF, microhardness measurements serve as a crucial indicator of material performance, as they directly correlate to the mechanical properties, durability, and reliability of the as-built structures. This parameter not only provides insights into the quality and consistency of the fusion process but also aids in understanding the influence of various process parameters on the final microstructure. Fig. 6 shows the Vickers hardness values along with both scanning speed and hatch distance values. It is clear that the highest hardness value is attained as hatch distance equals 75 µm with 405.8 HV (see Table 5) while the lowest hardness value is observed as hatch distance equals 125 µm with 360.8 HV (see Table 5). There is no distinct relation between hardness and scanning speed in a specific hatch distance set; nevertheless, both hardness values are higher than as-built LPBF [50,51]. Vilaro et al. carried out a comprehensive study of the microstructural evolution of Ti6Al4V during the LPBF process. Their results indicate that slower cooling rates facilitate the formation of a balanced α+β phase microstructure. This equilibrium is achieved because reduced cooling rates allow sufficient time

Scanning Speed (mm/min)	Hatch distance (µm)			
	50	75	100	125
800	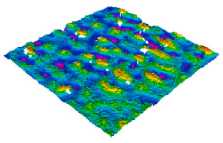 Ra= 25.497 µm E_s= 57 J/mm^2	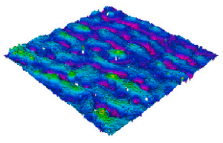 Ra= 36.364 µm E_s= 38 J/mm^2	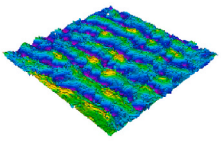 Ra= 35.948 µm E_s= 28.5 J/mm^2	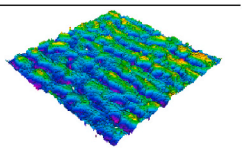 Ra= 34.903 µm E_s= 22.8 J/mm^2
1200	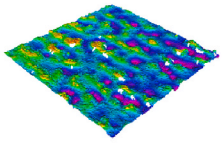 Ra= 30.599 µm E_s= 38 J/mm^2	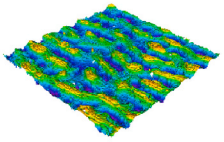 Ra= 36.761 µm E_s= 25.33 J/mm^2	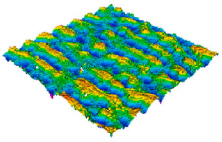 Ra= 39.440 µm E_s= 19 J/mm^2	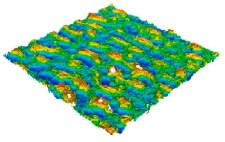 Ra= 34.331 µm E_s= 15.2 J/mm^2
1600	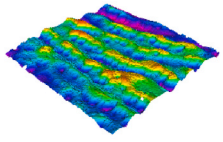 Ra= 34.696 µm E_s= 28.5 J/mm^2	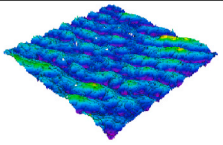 Ra= 36.914 µm E_s= 19 J/mm^2	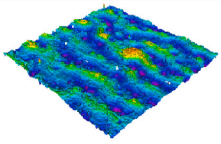 Ra= 29.060 µm E_s= 14.25 J/mm^2	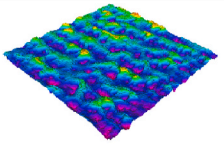 Ra= 25.402 µm E_s= 11.4 J/mm^2
2000	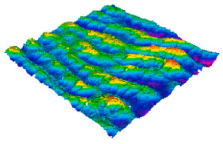 Ra= 39.549 µm E_s= 22.8 J/mm^2	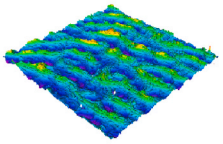 Ra= 37.543 µm E_s= 15.2 J/mm^2	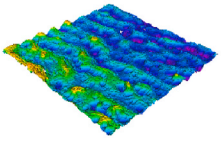 Ra= 27.750 µm E_s= 11.4 J/mm^2	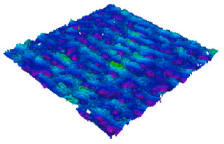 Ra= 26.324 µm E_s= 9.12 J/mm^2

Fig. 7. Top surface roughness of Ti6Al4V samples produced with the laser of 38W for different scanning speeds and hatch distances.

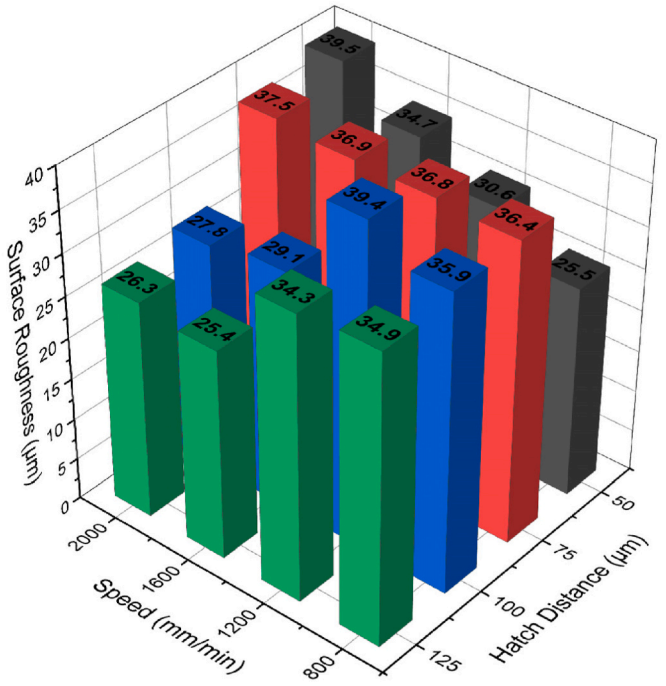

Fig. 8. Comparison chart of surface roughness of Ti6Al4V samples produced with the 38W laser for different scanning speeds and hatch distances.

for the β phase to transform into both α and β phases, resulting in a more homogeneous distribution of these phases throughout the material. Such a microstructure is associated with improved mechanical properties, including increased hardness and improved ductility, due to the uniform dispersion of the α and β phases [53]. As average values for hardness results are 387.925 HV, 390.95 HV, 376.95 HV, and 376.55 HV for hatch distances 50 µm, 75 µm, 100 µm, and 125 µm respectively. It is understood that lower hatch distances such as 50 and 75 µm demonstrate better hardness values compared to 100 and 125 µm.

Table 5 reveals that two samples that have nearly the same NED values express similar hardness results. For example, samples that are fabricated following process parameters such as hatch distance of 100 µm/scanning speed of 1600 mm/min and hatch distance of 125 µm/scanning speed of 1200 mm/min have 42.64 and 45.49 respectively. Also, this similarity is observed in other samples which were fabricated following process parameters such as a hatch distance of 50 µm/scanning speed of 1200 mm/min and hatch distance of 75 µm/scanning speed of 800 mm/min like 388.1 HV and 392.6 HV hardness results. Nevertheless, this cannot be extrapolated to all sets of samples, given the inconsistency between samples with similar NED values, which do not always yield comparable hardness results (see 75HD2000V and 100HD1600V in Table 5).

3.3.3. Surface roughness measurements

Surface roughness plays a pivotal role in determining the fatigue strength of LPBF-fabricated parts, often surpassing the influence of microstructure alone. This roughness arises from factors such as build orientation, powder particle characteristics, rapid solidification effects, and the inherent "staircase" layering effect. Fig. 7 shows the surface roughness of Ti6Al4V samples produced with the laser of 38 W with different scanning speeds and hatch distances. The top surface roughness of as-built LPBF samples exhibits lower values compared to DPM Ti6Al4V samples [49,54,55]. This discrepancy can be attributed to the relatively larger laser spot size employed in DPM compared to LPBF [43,54,55]. In their work, Yang et al. observed that the largest laser spot size, which is 0.4 mm, resulted in a surface that was rougher than that produced by a smaller spot size [56]. The top surface roughness of the samples was discussed in terms of a surface energy density calculation, which is illustrated in Equation (2). When Fig. 7 is examined, it is seen that the surface roughness value for all samples is in the range of 25–40 µm. For hatch values of 50 and 75 µm, it is observed that as the scanning speed increased, in other words, as the surface energy density values decrease, the top surface roughness increase. Furthermore, it is demonstrated that an increase in the number of laser tracks, resulting from excessive melt pool overlap, can lead to a reduction in surface roughness [57]. This shows that high surface energy value has a significant effect on the roughness of the material surface quality. On the other hand, no correlation is observed between the varies in speed and top surface roughness for hatch distances of 100 and 125 µm. It is also seen that the sample with the best top surface roughness value among all samples was the sample with 125 µm hatch distance and 1600 mm/min scanning speed (i.e., 11.4 J/mm^2). In addition, the top surface roughness values of samples with high hatch distance and high-speed values are generally lower than the others. This shows that a low surface energy density value has positive effects on the top surface roughness of Ti6Al4V.

Fig. 8 shows the variation of top surface roughness along with scanning speed for each hatch distance set. It is clear that top surface roughness increases from 800 to 1200 mm/min, then decreases to 2000 mm/min as hatch distance equals 100 or 125 µm. The top surface roughness diminishes at elevated scanning speeds due to the poor melt pool overlap for high hatch distance values (100 and 125 µm) [58]. A slight increase in top surface roughness is observed when the hatch distance was set to 125 µm and the scanning speed was 2000 mm/min. Top surface roughness on hatch distance of 75 µm samples fluctuate around 36 µm and it was not affected by different scanning speeds. Top surface roughness for samples with 50 µm hatch distance increase with scanning speed and maximum roughness value is obtained with the following parameters 50 µm of hatch distance and 2000 mm/min of scanning speed. It can be concluded that the minimum top surface

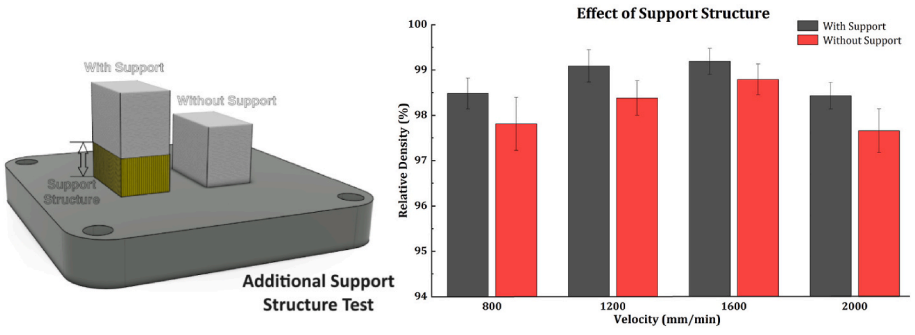

Fig. 9. a) Support structure test illustration and b) effect of support comparison chart.

Table 6
Effect of support structure overall comparison result table.

Specimen name	Support	Relative density (%)	Porosity Sizes (μm)
30LH, 100HD, 38P, 800V	Yes	98.48	22.40 (±8.57)
30LH, 100HD, 38P, 1200V	Yes	**99.09**	15.90 (±9.86)
30LH, 100HD, 38P, 1600V	Yes	**99.19**	14.40 (±7.04)
30LH, 100HD, 38P, 2000V	Yes	98.43	25.00 (±6.88)
30LH, 100HD, 38P, 800V	No	97.81	46.60 (±20.04)
30LH, 100HD, 38P, 1200V	No	**98.38**	56.50 (±19.74)
30LH, 100HD, 38P, 1600V	No	**98.79**	55.10 (±11.76)
30LH, 100HD, 38P, 2000V	No	97.66	51.50 (±16.53)

roughness result is observed on the sample with those process parameters 125 μm hatch distance and 1600 mm/min scanning speed.

3.4. Effect of support structure

Fig. 9a shows the visualisation of two samples with/without support together over the substrate. The yellow part under the sample placed on the left side shows the support structure. Fig. 9b presents relative density results for samples with/without support structure over varying scanning speeds. Support structures are primarily utilised in LPBF applications to enhance heat dissipation and minimise issues such as warpage or thermal distortion in printed parts [59]. Additionally, studies have shown that incorporating support structures (within support structure volume below component you have melted/sintered powder mixed with unmelted powder and air voids in powder bed) during LPBF can reduce the formation of columnar pores while increasing the relative density of H13 steel samples [60]. In experiments where power (38W), hatch distance (100 μm) and layer height (30 μm) is optimised and remained constant. Scanning speed has changed from 800 mm/min to 2000 mm/min with 400 mm/s intervals. The addition of support structures significantly improved the relative density of the samples across all scanning speeds. likely due to enhanced thermal management and reduced warping during the laser powder bed fusion process. The porosity sizes are also generally smaller across all scanning velocities. For example, at 800 mm/s, the porosity size decreases from 22.40 μm (±8.57) with support to 46.60 μm (±20.04) without support. Similarly, at 1200 mm/s, the porosity size is 15.90 μm (±9.86) with support, compared to 56.50 μm (±19.74) without support (se e Table 6). The same trend is observed for velocities of 1600 mm/s and 2000 mm/s, where the use of support results in slightly lower porosity sizes. This indicates that the presence of support structures contributes to a more uniform and reduced porosity distribution. Moreover, the use of low-density support structures restricted heat transfer from the main printed part to the substrate, allowing the part to retain more heat and thus experience slower cooling rates, which further enhances its density. Furthermore, Table 6 clearly illustrates the relative density of samples subjected to various process parameters.

3.5. Microstructural investigation

Following a systematic investigation to determine the optimum process parameters a set of conditions yielded the most favourable outcomes are identified. The subsequent research presents an analysis of this microstructure, focusing on the relationship between the selected process parameters and key features such as grain size, phase distribution, and morphological attributes. According to optimal process parameters of DPM, which is laser power 38 W, scanning speed 1600 mm/min, hatch distance 100 μm and layer height 30 μm. Fig. 10 shows

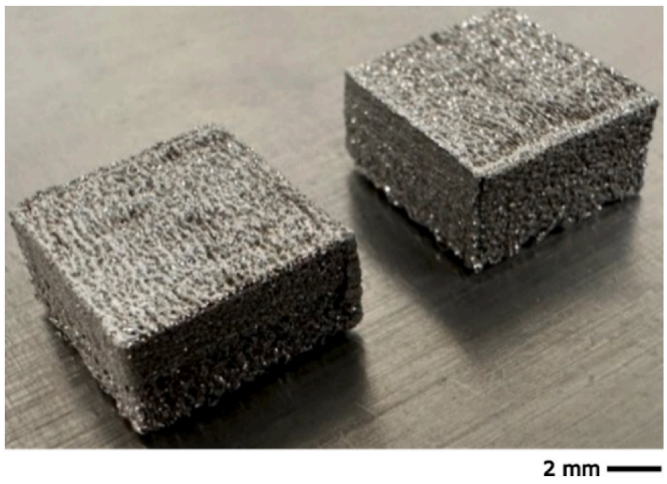

Fig. 10. DPM manufactured Ti6Al4V parts with best process parameters.

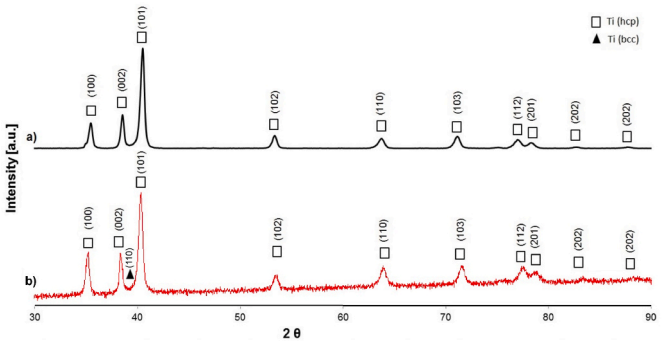

Fig. 11. The XRD (X-ray diffraction) patterns for Ti6Al4V alloy obtained in the a) LPBF [64] and b) DPM sample used in this study.

samples with the best process parameters. Then, X-ray diffraction (XRD) and EBSD analysis are conducted from these samples.

The phase composition proposed from metallographic observations is confirmed by XRD diffraction patterns in Fig. 11. Literature study [61] and the Powder Diffraction File (PDF) maps 00-044-1294 [62] 00-009-0098 [63] are used to assign the crystallographic structure of the XRD peaks, as typical maps for rapidly prototyped Ti6Al4V alloys are not yet available in the reference databases. No β-Ti is identified for the LPBF material as all peaks are assigned to hcp titanium. Similar to the DPM samples, the result is very close to the LPBF samples, but due to the slow cooling rate, only a very small percent of the 110-degree crystal orientation (β-Ti) structure is observed in the XRD analysis.

To understand of the microstructural morphology of the best parameters on the printed part, EBSD on the frontal xz-, lateral yz-, and horizontal xy-planes of the stress-relieved parts are carried out. The α orientation maps from lateral yz-planes indicate that there are fewer α colonies present in the microstructure, different from that observed for LPBF Ti6Al4V in the as-built condition [52]. The corresponding α contour pole figures show that the α texture is stronger as a result of the multiple variants that have formed within the β columnar grains. The reconstruction of the crystallographic orientation of the corresponding β phase shows that the β grains grow epitaxially through successive deposited layers. The prior-β phase has a dominant solidification texture with different orientation the grain growth direction. This is because of the slow cooling rate of the DPM system compared to LPBF. The results easily represent the differences reported for LPBF Ti6Al4V in the as-built condition [52].

The IPF colours are shown in the build direction. The IPF of the original scan is shown in Fig. 12b. The maximum Feret diameter is used

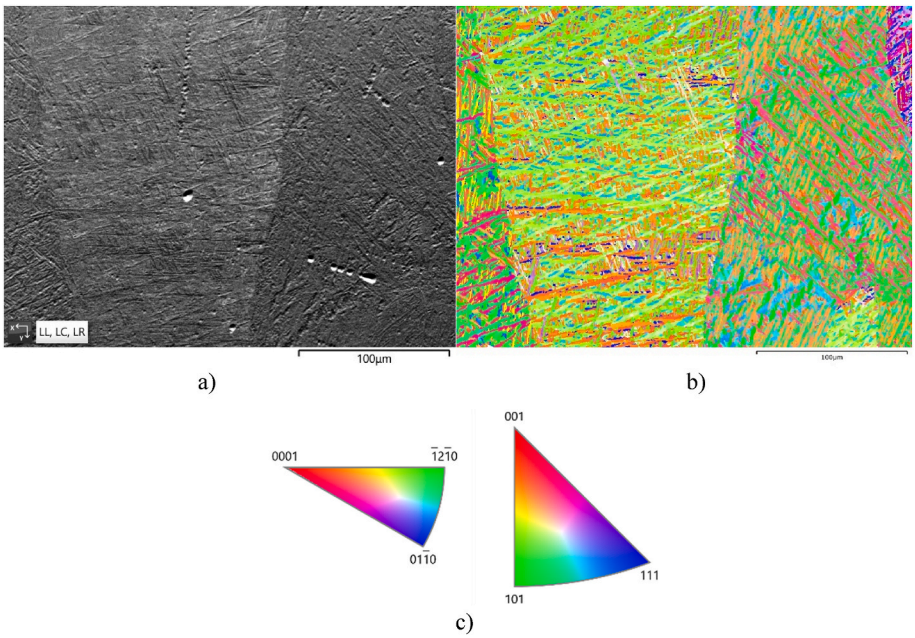

Fig. 12. a) FSD image of EBSD specimen and b) IPF ZColor microstructure views c) α and β grains orientation on EBSD index mapping.

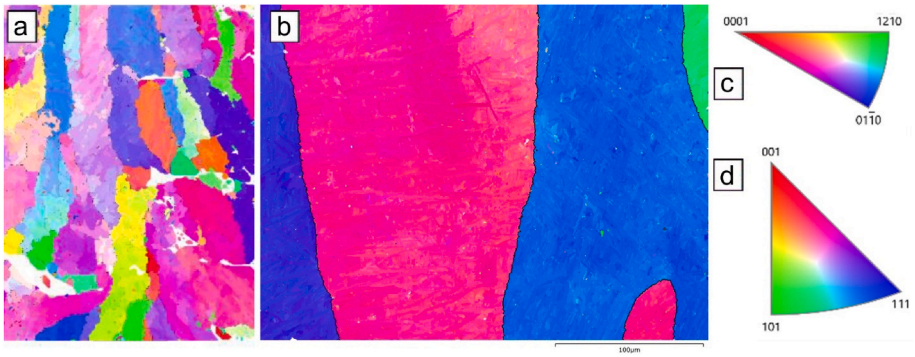

Fig. 13. a) Reconstructed parent β grains for LPBF example [65], b) reconstructed parent β grains for DPM zone c) color key for β phase and d) color key for α phase.

to evaluate the size of the α/α′ lamellae in the different zones. The average maximum Feret diameter for DPM and LPBF zones are measured as 9.73 µm and 6.61 µm [65], Detection of the β phase in EBSD analysis, the amount of β detected by EBSD is 0.34% in volume of the desired scanning zones. The inverse pole figure obtained from Fig. 12b, shows needle-shaped textures, indicating the presence of acicular α-martensite [66,67]. The size of acicular α-martensite has an average grain width of 1.2–3.15 µm and a length of 8–99.6 µm. In addition, the acicular α-martensite forms complex β-columnar grains that occur along the direction of growth with a size of 100 s µm.

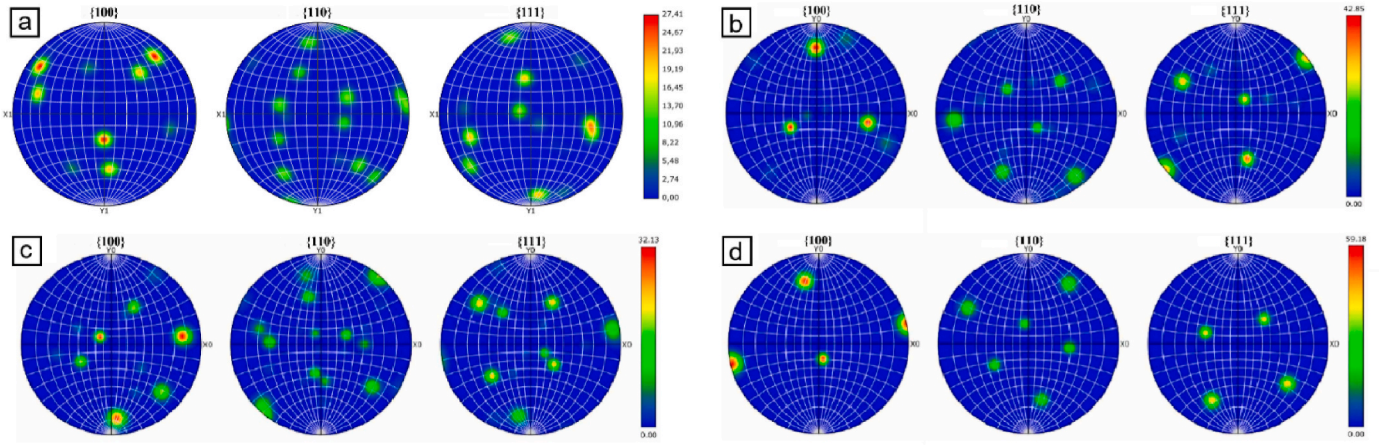

Fig. 14. a) Pole figures of reconstructed parent β grains from a) DPM zone, b) LPBF example T1 [68], c) LPBF example T2 [68] and d) LPBF example T3 [68].

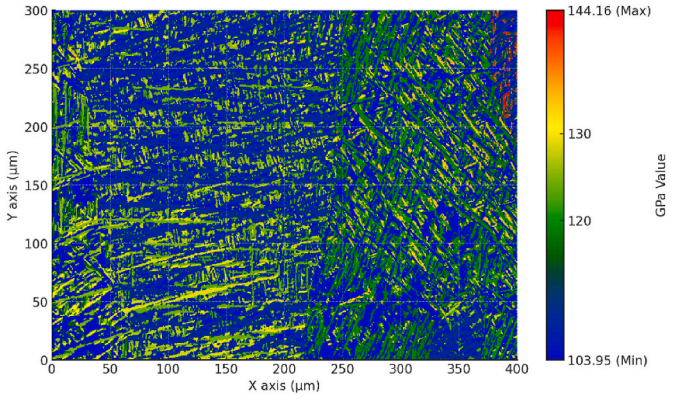

Fig. 15. Young's modulus map from a Ti6Al4V sample, determined from crystal orientation measured by EBSD (20 kV, Symmetry detector, 250 nm step size, 300 µm × 400 µm scanned area). Young's modulus is calculated assuming a tensile direction along the z-axis.

The IPF of parent β grains reconstructed from Fig. 13b according to the Burgers orientation relationship is given in Fig. 13b. The grain area is used to evaluate parent β grain size, as parent β grains are much larger than α laths. The average grain area is measured as 13743 μm^2 for DPM, and 454 μm^2 for LPBF regions [65]. This indicates that parent β grains in the DPM zone are approximately ×30 times larger than in the LPBF zone. The parent β grains observed within the DPM zone are not fully captured during the scanning process, indicating that the imaging was incomplete. This incomplete scanning suggests that the actual size of the DPM grains exceeds the previously calculated values. The findings imply that the current calculations may underestimate the true dimensions of the DPM grains.

Fig. 14 shows the textures of the samples in pole figures. It shows that all samples, including LPBF, have a stronger texture in the {100} orientation than in the {110} and {111} orientations. The maximum texture intensities of DPM, LPBF produced T1, T2 and T3 samples observed in the {100} orientations are 27.41, 42.85, 32.13 and 59.18 respectively, indicating that DPM has the least concentrated texture. This is because the cooling rate of DPM is less than $<10^4$ °C/s compared to the cooling rate of LPBF which is $\sim10^7$ °C/s [19,20]. The cooling rate affects the grain growth mechanisms, resulting in different grain orientations and texture intensities.

Various schemes exist for estimating the bulk elastic properties of anisotropic polycrystalline materials, the most common of which is the Voigt-Reuss-Hill approximation. Using the texture distribution obtained by EBSD, the stiffness tensor for the hexagonal α-phase is transformed into the orthorhombic macroscopic tensor. To investigate this further, the measured EBSD data is used to predict the macroscopic elastic tensor of the measured specimen. Once the EBSD data has been acquired, it is then possible to combine it with the Voigt-Reuss-Hill method described above to calculate the average elastic tensor. The initial hexagonal tensors are defined as C11, C12, C13, C33, C44 with the value of 160, 90, 66, 181 and 46,5 GPa respectively [69].

Fig. 15 shows the averaged Young's modulus distribution over the entire scan area, calculated using the Hill method from the EBSD data shown in Fig. 14a. The Hill method is an arithmetic average of the upper and lower bounds given by the Reuss and Voigt methods. With this method, calculated bounds for Voigt 115,78 GPa, Reuss 112,24 GPa and the Hill is 114,01 GPa from Fig. 15 overall scanning area. Young's Modulus of the LPBF samples ranging from 102 to 114 GPa for Ti6Al4V alloy, as reported in various studies [70–76]. The rapid cooling associated with LPBF often results in the retention of metastable phases, particularly the martensitic α′ phase, which is known to exhibit relatively lower stiffness. This variation can be attributed to differences in the microstructural development caused by the cooling rates. In LPBF processing, the rapid cooling leads to the formation of martensitic

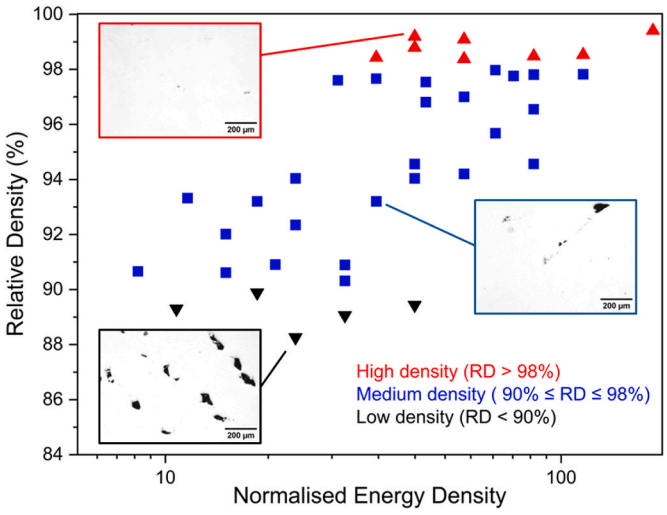

Fig. 16. Relative density-NED graph of DPM manufactured Ti6Al4V samples.

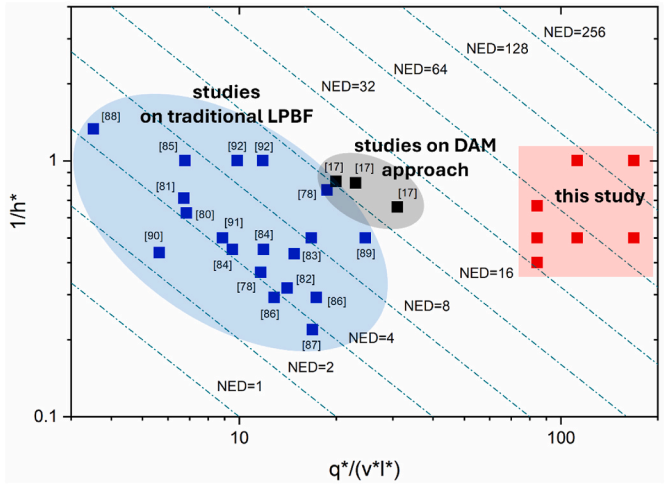

Fig. 17. NED mapping sample produced by best process parameters in this study and literature LPBF [78–92] and DAM study [17].

structures due to their less organized atomic arrangement, tend to have a lower modulus. Conversely, slower cooling rates, as applied in the DPM samples, facilitate the complete transformation of β-phase to α and β phases, which generally results in higher stiffness. The higher Young's modulus of the slow-cooled DPM samples compared to the LPBF manufactured samples is likely due to the more stable microstructure resulting from the slower cooling rate. This finding indicates that the cooling rate plays a critical role in determining the mechanical properties of Ti6Al4V alloy, with slower rates producing a material that is stiffer and more resistant to deformation.

3.6. Summary of obtained results and literature comparison of the samples produced by optimum process parameters

The relative density-NED results obtained with different hatch, layer thickness, power, and speed parameters are presented in Fig. 16. In the figure, the values above 98% (red triangles) of the relative density, below 90% (black triangles) and between these values (blue squares) are referred to high, low and medium density, respectively. Additionally, representative optical images for high, medium, and low-density structures are provided. These graphical illustrations are designed to generate a parameter map that marks areas with densities over 98%. The

Table 7
Overall comparison of LPBF, DAM and DPM (this study) approaches.

Method	Relative density (%)	Surface roughness R_a (μm)	Hardness (HV)	Grain area (μm^2)	Young modulus (GPa)	NED	Ref
LPBF	≤99.9	2.6–8	280–443	454	102–114	3.7–14.6	[78–92]
DAM	≤99.3	3.8–58.7	225–235	5940	110–119	16.6–20.4	[16,17]
DPM	≤99.4	25.4–39.5	360–406	13743	112–116	34.1–170.6	this study

figure reveals that it is possible to achieve samples with densities exceeding 95% using a 38 W laser power and a 450 nm DPM approach, provided that the NED value is above 68. Furthermore, for samples with an NED value over 120, densities exceeding 99.4% have been demonstrated to be achievable. Similar to this study, Caglar et al. [17] achieved a relative density above 98% using nine 450 nm 4 W diode lasers, yielding a total laser power of 36 W, by applying a rescanning strategy. In addition, Alsaddah et al. [77] used ten 808 nm 5 W diode lasers, reaching a total laser power of 50 W, to reach a comparable relative density level (above 98%) by adding a heating module to the powder bed system. This indicates that with the DPM approach used in this study, the 38 W 450 nm diode lasers demonstrate a 24% higher efficiency in laser power compared to the 808 nm, 50 W DAM approach reported by Alsaddah et al. [77].

Fig. 17 and Table 7 show the NED mapping and overall comparison of the studies on traditional LPBF and DAM with the current DPM study. In Fig. 17 and Table 7, only the most dense samples from traditional LPBF and DAM studies in the literature, as well as samples with relative density values of 98% and above from this study, are considered. Accordingly, the densest samples are obtained with NED values ranging between 3.7 and 14.6 for samples produced by traditional LPBF systems, between 16.6 and 20.4 for the DAM approach, and between 34.1 and 170.6 in this study.

In Table 7, prepared based on the densest samples found in literature, the relative density, surface roughness, hardness, grain area, Young's modulus, and NED values obtained from the DPM approach in this study are compared with those from previous studies in the literature. In terms of surface roughness, this study exhibits higher top surface roughness compared to traditional LPBF, while remaining within the range of the DAM approach. When considering hardness values, this study achieves significantly higher hardness values than the DAM approach, while obtaining hardness values that are above average compared to traditional LPBF. Additionally, in terms of grain size, the DAM approach has a grain size area that is 13 times larger compared to the traditional LPBF approach, while the DPM approach used in this study exhibits a grain size area that is 30 times larger. When considering Young's modulus, the traditional LPBF approach exhibits a lower Young's modulus, while the DAM and DPM approaches yield similar results. This can be attributed to the lower cooling rates observed in the DAM and DPM approaches.

4. Conclusion

This study investigated the potential of DPM using an efficient short wavelength laser as an alternative to traditional LPBF for the fabrication of Ti6Al4V components. DPM laser hardware costs are significantly lower than traditional LPBF generating reduced melt pool solidification rates. This research focused on optimising key parameters such as laser power, hatch distance, layer thickness and scan speed to achieve high material density components of up to 99.41% with the pore size of 14.10 μm (±4.98).

LPBF samples achieve significantly smoother surfaces, with surface roughness (Ra) values ranging from 2.6 to 8 μm, compared to Diode Point Melting (DPM), which has a higher roughness range of 25.4–39.5 μm. However, this difference in roughness can be attributed to the laser spot sizes used in DPM, which typically use a larger rectangular spot of 100 × 150 μm, whereas LPBF uses smaller circular laser spot sizes of 30–50 μm. Consequently, the larger spot size in DPM inherently contributes to a rougher surface compared to the finer resolution achieved in LPBF. Optimal results in DPM, achieved at a hatch distance of 125 μm and a scan speed of 1600 mm/min, give surface roughness values of around 25 μm due to improved melt pool overlap.

The processes reduced cooling rates facilitated the formation of a unique texture orientation and grain structure of larger β-phase grains and formations of stable α + β phase grains, which contributed to an increase in hardness and stiffness compared to those typically observed in LPBF-produced parts. The grain size of Ti6Al4V samples fabricated using DPM was 30x times larger compared to those produced by LPBF. The microstructure observed had similar traits (example large parental β grains) to those produced LPBF with post heat treatment samples.

This study highlighted the viability of DPM as a cost effective, scalable alternative to LPBF for the manufacturing of Ti6Al4V components. Future work could further refine the DPM parameters, explore additional alloy systems and evaluate the long-term performance characteristics of DPM fabricated parts in real-world applications. The integration of in-situ monitoring and feedback control systems could also improve the reproducibility and consistency of DPM-produced parts, positioning DPM as an alternative to traditional LPBF technology in AM.

CRediT authorship contribution statement

Alkim Aydin: Formal analysis, Investigation, Methodology, Software, Visualization, Writing – original draft, Writing – review & editing. **Erhan Cetin:** Investigation, Methodology, Validation, Writing – original draft, Writing – review & editing. **S. Can Erman:** Investigation, Methodology, Visualization, Writing – original draft, Writing – review & editing. **Kamran Mumtaz:** Funding acquisition, Project administration, Supervision, Validation, Writing – review & editing.

Data availability

Data will be made available on request.

Declaration of competing interest

The authors declare that they have no known competing financial interests or personal relationships that could have appeared to influence the work reported in this paper.

Acknowledgment

This study was completed with support from the Turkish Government Ministry of Education, Cukurova University Unit of Scientific Research and Projects with project number FBA-2023-15352, TUBITAK-2219 postdoctoral fellowship support program with project number 1059B192300923 and UK Research and Innovation, Engineering and Physical Sciences Research Council (EPSRC) Grant EP/W024764/1.

References

[1] Kaikai X, Yadong G, Qiang Z. Comparison of traditional processing and additive manufacturing technologies in various performance aspects: a review. Arch Civ Mech Eng 2023;23:188. https://doi.org/10.1007/s43452-023-00699-3.
[2] Pereira T, V Kennedy J, Potgieter J. A comparison of traditional manufacturing vs additive manufacturing, the best method for the job. Procedia Manuf 2019;30:11–8. https://doi.org/10.1016/j.promfg.2019.02.003.

[3] Achillas C, Tzetzis D, Raimondo MO. Alternative production strategies based on the comparison of additive and traditional manufacturing technologies. Int J Prod Res 2017;55:3497–509. https://doi.org/10.1080/00207543.2017.1282645.

[4] Kan WH, Chiu LNS, Lim CVS, Zhu Y, Tian Y, Jiang D, Huang A. A critical review on the effects of process-induced porosity on the mechanical properties of alloys fabricated by laser powder bed fusion. J Mater Sci 2022;57:9818–65. https://doi.org/10.1007/s10853-022-06990-7.

[5] Volpato GM, Tetzlaff U, Fredel MC. A comprehensive literature review on laser powder bed fusion of Inconel superalloys. Addit Manuf 2022;55:102871. https://doi.org/10.1016/j.addma.2022.102871.

[6] Kiass E-M, Zarbane K, Beidouri Z. Optimizing AlSi10Mg Part Quality aspects in laser powder bed fusion: a literature review. Lasers in manufacturing and materials processing. 2024. https://doi.org/10.1007/s40516-024-00267-4.

[7] Ahmed N, Barsoum I, Haidemenopoulos G, Al-Rub RKA. Process parameter selection and optimization of laser powder bed fusion for 316L stainless steel: a review. J Manuf Process 2022;75:415–34. https://doi.org/10.1016/j.jmapro.2021.12.064.

[8] Konieczny B, Szczesio-Wlodarczyk A, Sokolowski J, Bociong K. Challenges of Co–Cr alloy additive manufacturing methods in dentistry—the current state of knowledge (systematic review). Materials 2020;13:3524. https://doi.org/10.3390/ma13163524.

[9] Liu S, Shin YC. Additive manufacturing of Ti6Al4V alloy: a review. Mater Des 2019;164:107552. https://doi.org/10.1016/j.matdes.2018.107552.

[10] Shipley H, McDonnell D, Culleton M, Coull R, Lupoi R, O'Donnell G, Trimble D. Optimisation of process parameters to address fundamental challenges during selective laser melting of Ti-6Al-4V: a review. Int J Mach Tools Manuf 2018;128:1–20. https://doi.org/10.1016/j.ijmachtools.2018.01.003.

[11] Liu Y, Yang Y, Wang D. A study on the residual stress during selective laser melting (SLM) of metallic powder. Int J Adv Des Manuf Technol 2016;87:647–56. https://doi.org/10.1007/s00170-016-8466-y.

[12] Xiao Z, Chen C, Zhu H, Hu Z, Nagarajan B, Guo L, Zeng X. Study of residual stress in selective laser melting of Ti6Al4V. Mater Des 2020;193:108846. https://doi.org/10.1016/j.matdes.2020.108846.

[13] Karp JH, Ostroverkhov V, Bogdan D, Graham M, Mccarthy B, Carter W. Area melting with multi-laser arrays to increase build rate for metal powder bed fusion additive manufacturing. In: Helvajian H, Gu B, Chen H, editors. Laser 3D manufacturing. VI; 2019. p. 8. https://doi.org/10.1117/12.2513892. SPIE.

[14] Bernsmann J-SL, Hillebrandt S, Rommerskirchen M, Bold S, Schleifenbaum JH. On the use of metal sinter powder in laser powder bed fusion processing (PBF-lb/M). Materials 2023;16:5697. https://doi.org/10.3390/ma16165697.

[15] Zavala-Arredondo M, Boone N, Willmott J, Childs DTD, Ivanov P, Groom KM, Mumtaz K. Laser diode area melting for high speed additive manufacturing of metallic components. Mater Des 2017;117:305–15. https://doi.org/10.1016/j.matdes.2016.12.095.

[16] Alsaddah M, Khan A, Groom K, Mumtaz K. Use of 450-808 nm diode lasers for efficient energy absorption during powder bed fusion of Ti6Al4V. Int J Adv Des Manuf Technol 2021;113:2461–80. https://doi.org/10.1007/s00170-021-06774-4.

[17] Caglar H, Liang A, Groom K, Mumtaz K. Multi-laser powder bed fusion of Ti6Al4V: diode area melting utilizing low-power 450 nm diode lasers. J Mater Process Technol 2024:118303. https://doi.org/10.1016/j.jmatprotec.2024.118303.

[18] Tan C, Wang D, Ma W, Zhou K. Ultra-strong bond interface in additively manufactured iron-based multi-materials. Mater Sci Eng, A 2021;802:140642. https://doi.org/10.1016/j.msea.2020.140642.

[19] Hooper PA. Melt pool temperature and cooling rates in laser powder bed fusion. Addit Manuf 2018;22:548–59. https://doi.org/10.1016/j.addma.2018.05.032.

[20] Yang J, Yu H, Yin J, Gao M, Wang Z, Zeng X. Formation and control of martensite in Ti-6Al-4V alloy produced by selective laser melting. Mater Des 2016;108:308–18. https://doi.org/10.1016/j.matdes.2016.06.117.

[21] Gong J, Wei K, Liu M, Song W, Li X, Zeng X. Microstructure and mechanical properties of AlSi10Mg alloy built by laser powder bed fusion/direct energy deposition hybrid laser additive manufacturing. Addit Manuf 2022;59:103160. https://doi.org/10.1016/j.addma.2022.103160.

[22] Simonelli M, Tse YY, Tuck C. Effect of the build orientation on the mechanical properties and fracture modes of SLM Ti–6Al–4V. Mater Sci Eng, A 2014;616:1–11. https://doi.org/10.1016/j.msea.2014.07.086.

[23] Al-Bermani SS, Blackmore ML, Zhang W, Todd I. The origin of microstructural diversity, texture, and mechanical properties in electron beam melted Ti-6Al-4V. Metall Mater Trans 2010;41:3422–34. https://doi.org/10.1007/s11661-010-0397-x.

[24] Qu S, Ding J, Fu J, Fu M, Zhang B, Song X. High-precision laser powder bed fusion processing of pure copper. Addit Manuf 2021;48:102417. https://doi.org/10.1016/j.addma.2021.102417.

[25] Domine A, Dembinski L, Vitu L, Fenineche N. 18 Karat yellow gold single-tracks manufactured by Laser Powder Bed Fusion (LPBF): 1 064 nm and 515 nm laser comparison. Gold Bull 2023;56:53–8. https://doi.org/10.1007/s13404-023-00337-z.

[26] Materials A. Titanium alloys - Ti6Al4V grade 5. https://Www.Azom.Com/Article.Aspx?ArticleID=1547; 2002.

[27] Schneider CA, Rasband WS, Eliceiri KW. NIH Image to ImageJ: 25 years of image analysis. Nat Methods 2012;9:671–5. https://doi.org/10.1038/nmeth.2089.

[28] Gülenç İT, Bai M, Mitchell RL, Todd I, Inkson BJ. In situ TiC reinforced Ti6Al4V matrix composites manufactured via selective laser melting. Rapid Prototyp J 2024;30:378–92. https://doi.org/10.1108/RPJ-01-2023-0027.

[29] Kan WH, Gao M, Zhang X, Liang E, Chiu NSL, Lim CVS, Huang A. The influence of porosity on Ti-6Al-4V parts fabricated by laser powder bed fusion in the pursuit of process efficiency. Int J Adv Des Manuf Technol 2022;119:5417–38. https://doi.org/10.1007/s00170-021-08374-8.

[30] Snow Z, Nassar AR, Reutzel EW. Invited Review Article: review of the formation and impact of flaws in powder bed fusion additive manufacturing. Addit Manuf 2020;36:101457. https://doi.org/10.1016/j.addma.2020.101457.

[31] du Plessis A. Effects of process parameters on porosity in laser powder bed fusion revealed by X-ray tomography. Addit Manuf 2019;30:100871. https://doi.org/10.1016/j.addma.2019.100871.

[32] Rezaeifar H, Elbestawi M. Porosity formation mitigation in laser powder bed fusion process using a control approach. Opt Laser Technol 2022;147:107611. https://doi.org/10.1016/j.optlastec.2021.107611.

[33] Thomas M, Baxter GJ, Todd I. Normalised model-based processing diagrams for additive layer manufacture of engineering alloys. Acta Mater 2016;108:26–35. https://doi.org/10.1016/j.actamat.2016.02.025.

[34] Shipley H, McDonnell D, Culleton M, Coull R, Lupoi R, O'Donnell G, Trimble D. Optimisation of process parameters to address fundamental challenges during selective laser melting of Ti-6Al-4V: a review. Int J Mach Tools Manuf 2018;128:1–20. https://doi.org/10.1016/j.ijmachtools.2018.01.003.

[35] Guo Q, Zhao C, Qu M, Xiong L, Escano LI, Hojjatzadeh SMH, Parab ND, Fezzaa K, Everhart W, Sun T, Chen L. In-situ characterization and quantification of melt pool variation under constant input energy density in laser powder bed fusion additive manufacturing process. Addit Manuf 2019;28:600–9. https://doi.org/10.1016/j.addma.2019.04.021.

[36] Cepeda-Jiménez CM, Potenza F, Magalini E, Luchin V, Molinari A, Pérez-Prado MT. Effect of energy density on the microstructure and texture evolution of Ti-6Al-4V manufactured by laser powder bed fusion. Mater Charact 2020;163:110238. https://doi.org/10.1016/j.matchar.2020.110238.

[37] Watring DS, Benzing JT, Hrabe N, Spear AD. Effects of laser-energy density and build orientation on the structure–property relationships in as-built Inconel 718 manufactured by laser powder bed fusion. Addit Manuf 2020;36:101425. https://doi.org/10.1016/j.addma.2020.101425.

[38] Scipioni Bertoli U, Wolfer AJ, Matthews MJ, Delplanque J-PR, Schoenung JM. On the limitations of volumetric energy density as a design parameter for selective laser melting. Mater Des 2017;113:331–40. https://doi.org/10.1016/j.matdes.2016.10.037.

[39] Buhairi MA, Foudzi FM, Jamhari FI, Sulong AB, Radzuan NAM, Muhamad N, Mohamed IF, Azman AH, Harun WSW, Al-Furjan MSH. Review on volumetric energy density: influence on morphology and mechanical properties of Ti6Al4V manufactured via laser powder bed fusion. Progress in Additive Manufacturing 2023;8:265–83. https://doi.org/10.1007/s40964-022-00328-0.

[40] Fiocchi J, Biffi CA, Scaccabarozzi D, Saggin B, Tuissi A. Enhancement of the damping behavior of Ti 6 Al 4 V alloy through the use of trabecular structure produced by selective laser melting. Adv Eng Mater 2020;22. https://doi.org/10.1002/adem.201900722.

[41] Amano H, Yamaguchi Y, Ishimoto T, Nakano T. Reduction of spatter generation using atmospheric gas in laser powder bed fusion of Ti–6Al–4V. Mater Trans 2021;62. https://doi.org/10.2320/matertrans.MT-M2021059. MT-M2021059.

[42] Xu W, Brandt M, Sun S, Elambasseril J, Liu Q, Latham K, Xia K, Qian M. Additive manufacturing of strong and ductile Ti–6Al–4V by selective laser melting via in situ martensite decomposition. Acta Mater 2015;85:74–84. https://doi.org/10.1016/j.actamat.2014.11.028.

[43] Zhu Y, Chen X, Zou J, Yang H. Sliding wear of selective laser melting processed Ti6Al4V under boundary lubrication conditions. Wear 2016;368–369:485–95. https://doi.org/10.1016/j.wear.2016.09.020.

[44] Khorasani A, Gibson I, Goldberg M, Littlefair G. On the role of different annealing heat treatments on mechanical properties and microstructure of selective laser melted and conventional wrought Ti-6Al-4V. Rapid Prototyp J 2017;23:295–304. https://doi.org/10.1108/RPJ-02-2016-0022.

[45] Vrancken B, Thijs L, Kruth J-P, Van Humbeeck J. Heat treatment of Ti6Al4V produced by selective laser melting: microstructure and mechanical properties. J Alloys Compd 2012;541:177–85. https://doi.org/10.1016/j.jallcom.2012.07.022.

[46] Kaschel FR, Celikin M, Dowling DP. Effects of laser power on geometry, microstructure and mechanical properties of printed Ti-6Al-4V parts. J Mater Process Technol 2020;278:116539. https://doi.org/10.1016/j.jmatprotec.2019.116539.

[47] Khorasani AM, Gibson I, Ghasemi A, Ghaderi A. A comprehensive study on variability of relative density in selective laser melting of Ti-6Al-4V. Virtual Phys Prototyp 2019;14:349–59. https://doi.org/10.1080/17452759.2019.1614198.

[48] Vandenbroucke B, Kruth J. Selective laser melting of biocompatible metals for rapid manufacturing of medical parts. Rapid Prototyp J 2007;13:196–203. https://doi.org/10.1108/13552540710776142.

[49] Li Z, Kucukkoc I, Zhang DZ, Liu F. Optimising the process parameters of selective laser melting for the fabrication of Ti6Al4V alloy. Rapid Prototyp J 2018;24:150–9. https://doi.org/10.1108/RPJ-03-2016-0045.

[50] Greco S, Gutzeit K, Hotz H, Kirsch B, Aurich JC. Selective laser melting (SLM) of AISI 316L—impact of laser power, layer thickness, and hatch spacing on roughness, density, and microhardness at constant input energy density. Int J Adv Des Manuf Technol 2020;108:1551–62. https://doi.org/10.1007/s00170-020-05510-8.

[51] Li X, Liu Y, Tan C, Zou Y. Porosity formation mechanisms, microstructure evolution and mechanical performance of AlMgScZr alloy fabricated by laser powder bed fusion: effect of hatch distance. J Manuf Process 2023;94:107–19. https://doi.org/10.1016/j.jmapro.2023.03.047.

[52] Sufiiarov VSh, Popovich AA, Borisov EV, Polozov IA, Masaylo DV, Orlov AV. The effect of layer thickness at selective laser melting. Procedia Eng 2017;174:126–34. https://doi.org/10.1016/j.proeng.2017.01.179.
[53] Vilaro T, Colin C, Bartout JD. As-fabricated and heat-treated microstructures of the Ti-6Al-4V alloy processed by selective laser melting. Metall Mater Trans 2011;42:3190–9. https://doi.org/10.1007/s11661-011-0731-y.
[54] Oyesola M, Mpofu K, Mathe N, Fatoba S, Hoosain S, Daniyan I. Optimization of selective laser melting process parameters for surface quality performance of the fabricated Ti6Al4V. Int J Adv Des Manuf Technol 2021;114:1585–99. https://doi.org/10.1007/s00170-021-06953-3.
[55] Wang Z, Xiao Z, Tse Y, Huang C, Zhang W. Optimization of processing parameters and establishment of a relationship between microstructure and mechanical properties of SLM titanium alloy. Opt Laser Technol 2019;112:159–67. https://doi.org/10.1016/j.optlastec.2018.11.014.
[56] Yang X-H, Jiang C-M, Ho J-R, Tung P-C, Lin C-K. Effects of laser spot size on the mechanical properties of AISI 420 stainless steel fabricated by selective laser melting. Materials 2021;14:4593. https://doi.org/10.3390/ma14164593.
[57] Cherry JA, Davies HM, Mehmood S, Lavery NP, Brown SGR, Sienz J. Investigation into the effect of process parameters on microstructural and physical properties of 316L stainless steel parts by selective laser melting. Int J Adv Manuf Technol 2015;76:869–79. https://doi.org/10.1007/s00170-014-6297-2.
[58] Dong Z, Liu Y, Wen W, Ge J, Liang J. Effect of hatch spacing on melt pool and as-built quality during selective laser melting of stainless steel: modeling and experimental approaches. Materials 2018;12:50. https://doi.org/10.3390/ma12010050.
[59] Gan MX, Wong CH. Practical support structures for selective laser melting. J Mater Process Technol 2016;238:474–84. https://doi.org/10.1016/j.jmatprotec.2016.08.006.
[60] Kurzynowski T, Stopyra W, Gruber K, Ziółkowski G, Kuźnicka B, Chlebus E. Effect of scanning and support strategies on relative density of SLM-ed H13 steel in relation to specimen size. Materials 2019;12:239. https://doi.org/10.3390/ma12020239.
[61] Dinda GP, Song L, Mazumder J. Fabrication of Ti-6Al-4V scaffolds by direct metal deposition. Metall Mater Trans 2008;39:2914–22. https://doi.org/10.1007/s11661-008-9634-y.
[62] Sailer R, McCarthy C. Icdd grant-in-aid, ND. Fargo: North Dakota State University; 1993.
[63] Wyckoff RWG. Crystal structures. second ed., New Yoor. NY, USA: John Wiley & Sons, Inc.; 1963.
[64] Wysocki B, Maj P, Sitek R, Buhagiar J, Kurzydłowski K, Świętochowski W. Laser and electron beam additive manufacturing methods of fabricating titanium bone implants. Appl Sci 2017;7:657. https://doi.org/10.3390/app7070657.
[65] Caglar H, Aydin A, Gulenc IT, Groom K, Mumtaz K. Dual-laser powder bed fusion using 450 nm diode area melting and 1064 nm galvo-scanning fiber laser sources. Mater Des 2024;248:113511. https://doi.org/10.1016/j.matdes.2024.113511.
[66] Liu Y, Xu H, Zhu L, Wang X, Han Q, Li S, Wang Y, Setchi R, Wang D. Investigation into the microstructure and dynamic compressive properties of selective laser melted Ti–6Al–4V alloy with different heating treatments. Mater Sci Eng, A 2021;805:140561. https://doi.org/10.1016/j.msea.2020.140561.
[67] Kobryn PA, Semiatin SL. The laser additive manufacture of Ti-6Al-4V. JOM 2001;53:40–2. https://doi.org/10.1007/s11837-001-0068-x.
[68] Cui Y, Cai J, Li Z, Jiao Z, Hu L, Hu J. Effect of porosity on dynamic response of additive manufacturing Ti-6Al-4V alloys. Micromachines 2022;13:408. https://doi.org/10.3390/mi13030408.
[69] Tromans D. Elastic anisotropy of HCP metal crystals and polycrystals. Int. J. Res. Rev. Appl. 2011;6:462–83.
[70] Benedetti M, Torresani E, Leoni M, Fontanari V, Bandini M, Pederzolli C, Potrich C. The effect of post-sintering treatments on the fatigue and biological behavior of Ti-6Al-4V ELI parts made by selective laser melting. J Mech Behav Biomed Mater 2017;71:295–306. https://doi.org/10.1016/j.jmbbm.2017.03.024.
[71] Shunmugavel M, Polishetty A, Littlefair G. Microstructure and mechanical properties of wrought and additive manufactured Ti-6Al-4V cylindrical bars. Procedia Technology 2015;20:231–6. https://doi.org/10.1016/j.protcy.2015.07.037.
[72] Vrancken B, Thijs L, Kruth J-P, Van Humbeeck J. Heat treatment of Ti6Al4V produced by selective laser melting: microstructure and mechanical properties. J Alloys Compd 2012;541:177–85. https://doi.org/10.1016/j.jallcom.2012.07.022.
[73] Vilaro T, Colin C, Bartout JD. As-fabricated and heat-treated microstructures of the Ti-6Al-4V alloy processed by selective laser melting. Metall Mater Trans 2011;42:3190–9. https://doi.org/10.1007/s11661-011-0731-y.
[74] Gong H, Rafi K, Gu H, Janaki Ram GD, Starr T, Stucker B. Influence of defects on mechanical properties of Ti–6Al–4V components produced by selective laser melting and electron beam melting. Mater Des 2015;86:545–54. https://doi.org/10.1016/j.matdes.2015.07.147.
[75] Mower TM, Long MJ. Mechanical behavior of additive manufactured and powder metallurgy Ti6Al4V. In: Proceedings of the 13th world conference on titanium. Wiley; 2016. p. 1331–6. https://doi.org/10.1002/9781119296126.ch225.
[76] Facchini L, Magalini E, Robotti P, Molinari A, Höges S, Wissenbach K. Ductility of a Ti-6Al-4V alloy produced by selective laser melting of prealloyed powders. Rapid Prototyp J 2010;16:450–9. https://doi.org/10.1108/13552541011083371.
[77] Alsaddah M, Khan A, Groom K, Mumtaz K. Diode area melting of Ti6Al4V using 808 nm laser sources and variable multi-beam profiles. Mater Des 2022;215:110518. https://doi.org/10.1016/j.matdes.2022.110518.
[78] Vandenbroucke B, Kruth J. Selective laser melting of biocompatible metals for rapid manufacturing of medical parts. Rapid Prototyp J 2007;13:196–203. https://doi.org/10.1108/13552540710776142.
[79] Liu J, Sun Q, Zhou C, Wang X, Li H, Guo K, Sun J. Achieving Ti6Al4V alloys with both high strength and ductility via selective laser melting. Mater Sci Eng, A 2019;766:138319. https://doi.org/10.1016/j.msea.2019.138319.
[80] Li Z, Kucukkoc I, Zhang DZ, Liu F. Optimising the process parameters of selective laser melting for the fabrication of Ti6Al4V alloy. Rapid Prototyp J 2018;24:150–9. https://doi.org/10.1108/RPJ-03-2016-0045.
[81] Pal S, Gubeljak N, Hudak R, Lojen G, Rajtukova V, Predan J, Kokol V, Drstvensek I. Tensile properties of selective laser melting products affected by building orientation and energy density. Mater Sci Eng, A 2019;743:637–47. https://doi.org/10.1016/j.msea.2018.11.130.
[82] Zhu Y, Chen X, Zou J, Yang H. Sliding wear of selective laser melting processed Ti6Al4V under boundary lubrication conditions. Wear 2016;368–369:485–95. https://doi.org/10.1016/j.wear.2016.09.020.
[83] Mierzejewska ŻA, Hudák R, Sidun J. Mechanical properties and microstructure of DMLS Ti6Al4V alloy dedicated to biomedical applications. Materials 2019;12:176. https://doi.org/10.3390/ma12010176.
[84] Wang Z, Xiao Z, Tse Y, Huang C, Zhang W. Optimization of processing parameters and establishment of a relationship between microstructure and mechanical properties of SLM titanium alloy. Opt Laser Technol 2019;112:159–67. https://doi.org/10.1016/j.optlastec.2018.11.014.
[85] Du X, Chen J, She Y, Liu Y, Yang Y, Yang J, Dong S. Effect of process parameter optimization on morphology and mechanical properties of Ti6Al4V alloy produced by selective laser melting. Prog Nat Sci: Mater Int 2023;33:911–7. https://doi.org/10.1016/j.pnsc.2024.01.006.
[86] Xu W, Brandt M, Sun S, Elambasseril J, Liu Q, Latham K, Xia K, Qian M. Additive manufacturing of strong and ductile Ti–6Al–4V by selective laser melting via in situ martensite decomposition. Acta Mater 2015;85:74–84. https://doi.org/10.1016/j.actamat.2014.11.028.
[87] Fatemi A, Molaei R, Sharifimehr S, Phan N, Shamsaei N. Multiaxial fatigue behavior of wrought and additive manufactured Ti-6Al-4V including surface finish effect. Int J Fatigue 2017;100:347–66. https://doi.org/10.1016/j.ijfatigue.2017.03.044.
[88] Khorasani A, Gibson I, Goldberg M, Littlefair G. On the role of different annealing heat treatments on mechanical properties and microstructure of selective laser melted and conventional wrought Ti-6Al-4V. Rapid Prototyp J 2017;23:295–304. https://doi.org/10.1108/RPJ-02-2016-0022.
[89] Amano H, Yamaguchi Y, Ishimoto T, Nakano T. Reduction of spatter generation using atmospheric gas in laser powder bed fusion of Ti–6Al–4V. Mater Trans 2021;62. https://doi.org/10.2320/matertrans.MT-M2021059. MT-M2021059.
[90] Vrancken B, Thijs L, Kruth J-P, Van Humbeeck J. Heat treatment of Ti6Al4V produced by selective laser melting: microstructure and mechanical properties. J Alloys Compd 2012;541:177–85. https://doi.org/10.1016/j.jallcom.2012.07.022.
[91] Megahed S, Aniko V, Schleifenbaum JH. Electron beam-melting and laser powder bed fusion of Ti6Al4V: transferability of process parameters. Metals 2022;12:1332. https://doi.org/10.3390/met12081332.
[92] Luo Y, Wang M, Zhu J, Tu J, Jiao S. Microstructure and corrosion resistance of Ti6Al4V manufactured by laser powder bed fusion. Metals 2023;13:496. https://doi.org/10.3390/met13030496.